Simulation Study of the Wind Dynamics over Mont Tai during the Transition Periods

Iheng Tsai ·Meigen Zhang

28 April, Atmospheric Boundary Layer, EGU General Assembly 2021

Topography of Mont Tai Region

Terrain-induced circulations prevail in Tai-An city located on the southern foot of Mont Tai.

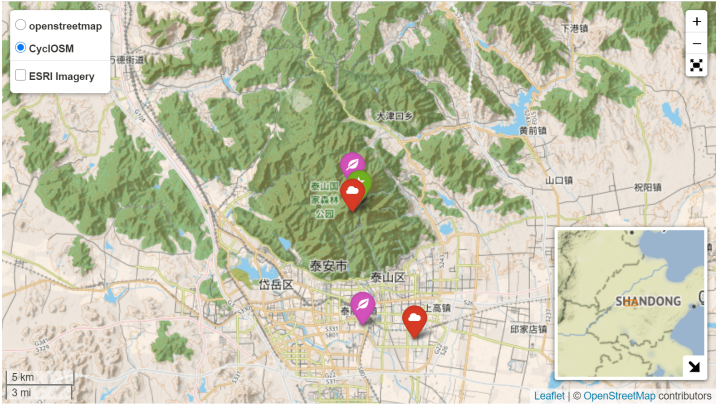

Figure 1

⇑ Please click on the map for more details

Motivation of Studying Thermally-driven Wind Transitions

- The wind development during morning or evening transitions may be **retained till** the quasi-stationary state of thermally-driven wind and causes ozone transport.
- The processes of genesis after lysis of thermally-driven flows **not spatially synchronise**. The physics behind these intriguing features enhances our interest.

Questions

1. How is nocturnal surface ozone enhancement in Tai-An city related to terrain-induced circulation? Can we quantify it?
2. Why is the flow reversal time different in different places?

RAMS v.6.2.12 Set-up

Table 1

DEM data	ASTER GDEM v.3	$\Delta x = 1'' \approx 30$ m, $\Delta z \approx 72$ m
Land cover data	MCD12Q1 v.6	$\Delta x \approx 500$ m, observed in 2018
NDVI data	PROBA-V NDVI 300m	$\Delta x \approx 333$ m, observed in 2018
Radiation	**Chen & Cotton**[a]	$\Delta t = 10$ min
Microphysics	Activates condensation of water vapor to cloud water wherever supersaturation is attained. (LEVEL $= 2$)	
Turbulent	Mellor-Yamada 2.5 level	IHORGRAD $= 1$, CSX(Z) $= 0.2$, AKMIN $= 0.02,\ 0.016,\ 1.0$.
Terrain Smoothing	**Reflected Envelope**	TOPTENH $\approx \sqrt{2}$
Land Surface	LEAF3	7 soil levels from 0.05 m to 0.8 m below ground, nudging from ERA5 Δt = 2 hr.
Time Differencing	time-split hybrid horizontal explicit and vertical implicit finite difference scheme	
Initialization	ERA5 reanalysis data	$\Delta x = 0.25°$, $\Delta t = 2$ hr.
Boundary conditions	the laterally outermost 5 points nudging to ERA5 with 1350-s damping, Klemp-Durran condition for the top boundary	

[a] The topographic effects of Chen & Cotton scheme consist of elevation, slope, aspect and self-shading.

RAMS Simulation

- Simulation time: 0000 LT 30 May to 2350 LT 15 July in 2018 (47 days).
- 45 vertical levels, Δz stretched from surface $\approx$ 60 m with ratio 1.09 to $H \approx$ 22.8 km.

Grid	$nx \times ny$	Δx (km)	Δt (s)
G1	70×69	8.0	20
G2	62×74	2.0	6.67
G3	98×122	0.5	2.22

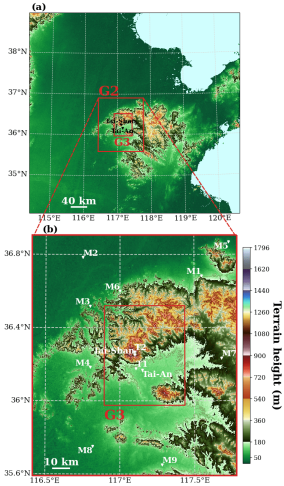

Figure 2: Domains

Transformation between σ_z Coordinates and Cartesian coordinates

$$z_{c,k} = \frac{H - z_G(x,y)}{H} z_{\sigma,k} + z_G(x,y) \tag{1}$$

$$w_{c,k} = w_{\sigma,k}\frac{H - z_G(x,y)}{H} + u_k \frac{\partial z_G(x,y)}{\partial x}\frac{H - z_{\sigma,k}}{H} + v_k \frac{\partial z_G(x,y)}{\partial y}\frac{H - z_{\sigma,k}}{H} \tag{2}$$

, where H is the height of model top, $z_G(x,y)$ is the topography.

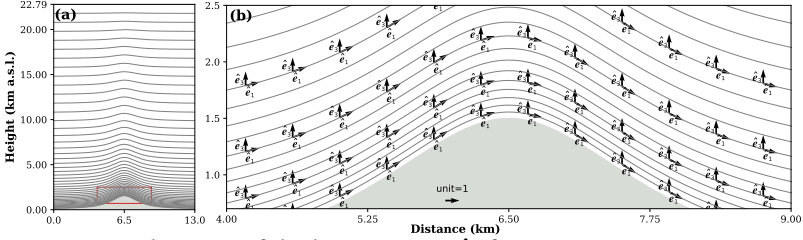

Figure 3: A schematic of the basis vectors $\hat{e}_i$ for contravariant components v^i in σ_z coordinate

Downward Extrapolation with Roughness Sublayer Effects

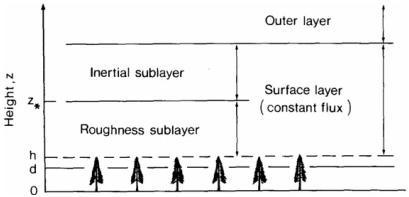

Figure 4: A schematic of atmospheric surface layer (ASL) and inertial sublayer (ISL), Roughness sublayer (RSL) and canopy layer (CL) from [1]

⇒ Temperature standard measured at 2 m a.g.l. likely within the RSL

Flux–gradient relationship for heat can be written as

$$\frac{\kappa(z-z_d)}{T_*}\frac{\partial T}{\partial z} = \Phi_H \approx \phi_H\left(\frac{z-z_d}{L}\right)\cdot\hat{\phi}_H\left(\frac{z-z_d}{z_*}\right) \quad (3)$$

, where Φ_H is the generalised similarity function, ϕ_H is the standard MOST similarity function and $\hat{\phi}_H$ is the Roughness sublayer profile function for heat. Dealing with $\hat{\phi}_H$, we follow De Ridder's empirical RSL parameterisation [2].

Select Valley-wind Days

Using hourly ERA5 800-hpa Geopotential Φ data to identify **weak synoptic pressure gradient** is given by [3]

$$\left|\frac{\Delta Z_g}{\Delta x}\right| \& \left|\frac{\Delta Z_g}{\Delta y}\right| \leqslant 4 \times 10^{-5} \tag{4}$$

, where $Z_g = \Phi/9.8$. Select dated more than 16 hours satisfy this condition. Using the observed short-wave radiation DR_{obs} to calculate **insolation deficit index** (IDI) is given by

$$\mathrm{IDI}(j) = \sum_{i=1}^{1440} \frac{DR_{skc}(i\Delta t, j) - DR_{obs}(i\Delta t, j)}{DR_{skc}(i\Delta t, j)} \leqslant 0.35 \tag{5}$$

, where j is the index of date, i is a dumb index to integrate daily insolation, $\Delta t = 1$ min, DR_{skc} is given by clear sky irradiance of `pvlib python` [4].

Results: The valley-wind days are 11, 12, 14, 15, 20, 24, 27 and 30 June in 2018 (8 out of 47 days of simulation).

Horizon Angle Algorithm

Consider a regular grid elevation data. The critical solar altitude angle is the source grid point $\boldsymbol{r}_j$ at ϕ azimuthal direction of the field grid point $\boldsymbol{r}_i$ precisely shading solar radiation, is defined as the horizon angle $\mathcal{H}_{i,j}(\boldsymbol{r}_i, \boldsymbol{r}_j, \phi)$, and is given as

$$\mathcal{H}_{i,j}(\boldsymbol{r}_i, \boldsymbol{r}_j, \phi) = \tan^{-1}\left(\frac{\boldsymbol{r}_j - \boldsymbol{r}_i}{z_{G,j} - z_{G,i}}\right) \tag{6}$$

We pre-calculated the maximum horizon angle $\mathcal{H}_i(\boldsymbol{r}_i, \phi)$ along eight azimuths of all grid points, and use solar azimuth angle $\phi_\odot$ to dictate sector with ϕ as bisector to call. If the maximum horizon angle $\mathcal{H}_i(\boldsymbol{r}_i, \phi)$ of point i is greater than the solar altitude angle $\theta_\odot$, point i would be shaded by surrounding terrain; *vice versa.*

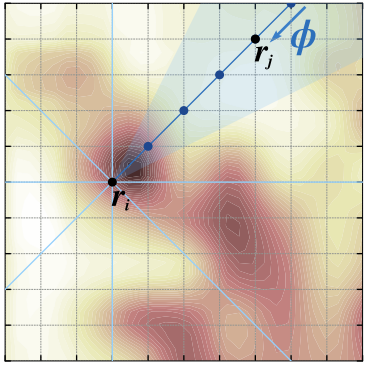

Figure 5: A schematic of calculating Horizon Angles

Model Performance

Table 2: Statistical performance metrics averaged over 13 sites

	MB	ME	FB	NMSE
10-m Wind Direction	-3.24 °	44.88 °	-	0.16
10-m Wind Speed	0.16 m s^{-1}	1.34 m s^{-1}	0.05	0.39
2-m Temperature	-0.44 ℃	1.83 ℃	-0.02	0.01

	MG	R^2	FAC_2	DACC (11.25°)	DACC (22.5°)	DACC (45°)
10-m Wind Direction	-	-	-	0.20	0.38	0.65
10-m Wind Speed	1.07	0.18	0.72	-	-	-
2-m Temperature	1.00	0.71	1.00	-	-	-

Results: Topographic Shading effect on Short-wave Radiation

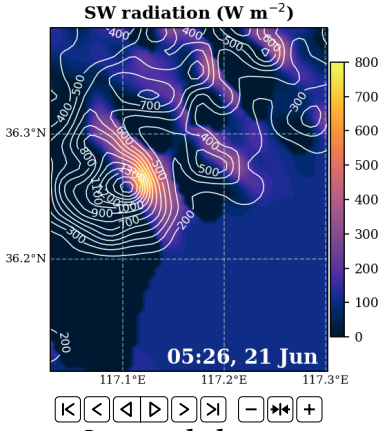

Seasonal change

from Summer Solstice to Winter Solstice

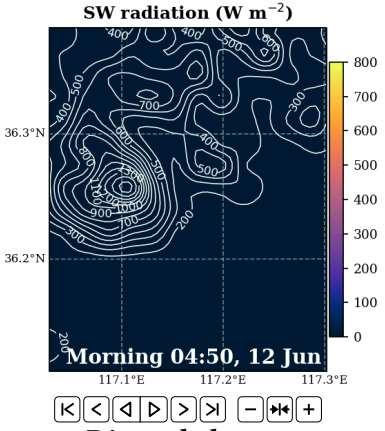

Diurnal change

Results: Flow Reversal during the Morning Transition

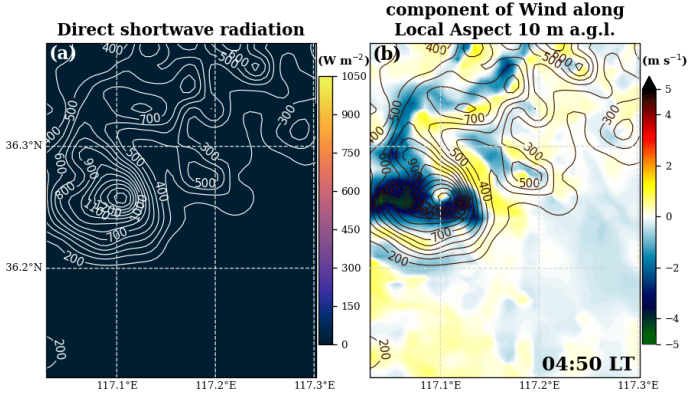

Results: Flow Reversal during the Evening Transition

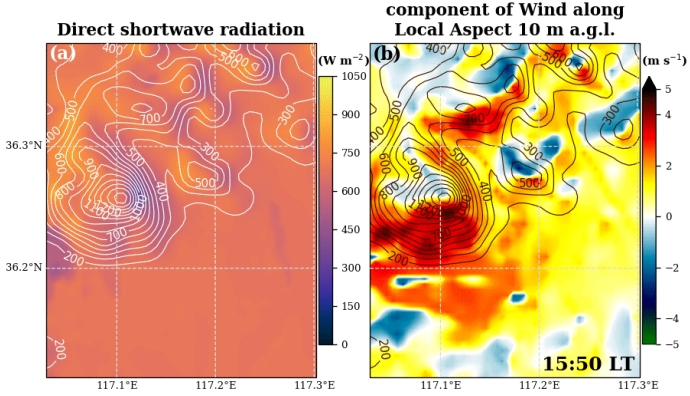

Results: Land-atmosphere Energy-transfer

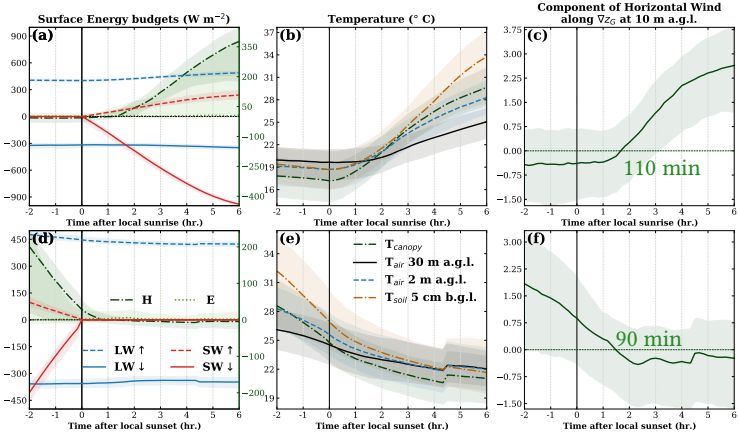

Figure 6: The evolution of land-atmosphere energy-transfer dynamics aligned by the local (a-c) sunrise or (d-f) sunset averaged over Mont Tai region

Conclusions

1. The results of our module show that the terrain shadowing has little effect on **isolated** Mont Tai, and it became negligible **1 hour** after sunrise.
2. As terrain shading mapping the sun path, shadow range changes with **seasons**.
3. The flow reversal follows the **self-shadowing** considering local sunrise and sunset for different aspects otherwise the **front formation** mechanism.
4. After variables were **referenced to local sunrise or sunset**, the energy transfer mechanisms during the transition periods are the sensible heat flux sign change, the vertical temperature gradient crossover and the flow reversal in order.

References I

[1] M. Raupach and B. Legg, "The uses and limitations of flux-gradient relationships in micrometeorology," *Agricultural Water Management*, vol. 8, no. 1-3, pp. 119–131, 1984. DOI: https://doi.org/10.1016/0378-3774(84)90049-0.

[2] K. D. Ridder, "Bulk transfer relations for the roughness sublayer," *Boundary-Layer Meteorology*, vol. 134, no. 2, pp. 257–267, 2009. DOI: 10.1007/s10546-009-9450-y.

References II

[3] M. Lehner, M. W. Rotach, and F. Obleitner, "A method to identify synoptically undisturbed, clear-sky conditions for valley-wind analysis," *Boundary-Layer Meteorology*, vol. 173, no. 3, pp. 435–450, 2019. DOI: 10.1007/s10546-019-00471-2.

[4] W. F. Holmgren, C. W. Hansen, and M. A. Mikofski, "Pvlib python: A python package for modeling solar energy systems," *Journal of Open Source Software*, vol. 3, no. 29, p. 884, 2018. DOI: 10.21105/joss.00884.

Simulation Study of the Wind Dynamics over Mont Tai during the Transition Periods

Iheng Tsai · Meigen Zhang

28 April, Atmospheric Boundary Layer,
EGU General Assembly 2021

Introduction

The continuity equation for local ozone concentration overnight:

$$\frac{\partial [O_3]}{\partial t} = -L_{O_3} - Dep_{O_3} - \left(\overline{u}\frac{\partial [O_3]}{\partial x} + \overline{v}\frac{\partial [O_3]}{\partial y}\right) - \overline{w}\frac{\partial [O_3]}{\partial z} + \frac{\partial}{\partial z}\left(K_z\frac{\partial [O_3]}{\partial z}\right) \quad (1)$$

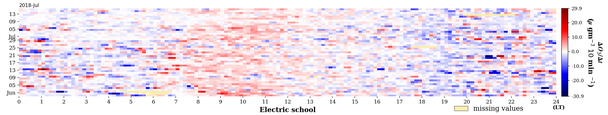

Figure 1: The rate of change of $[O_3]$ at a site in Tai-An city

Questions

- How is nocturnal surface ozone (NSO) enhancement related to terrain-induced circulation? Can we quantify it?
- The processes of genesis after lysis of thermally-driven flows not spatially synchronise. **Why is the flow reversal time different in different places?**

RAMS v.6.2.12 Analysis

- Updated DEM, land cover and NDVI dataset
- Simulation time: 0000 LT 30 May to 2350 LT 15 July in 2018

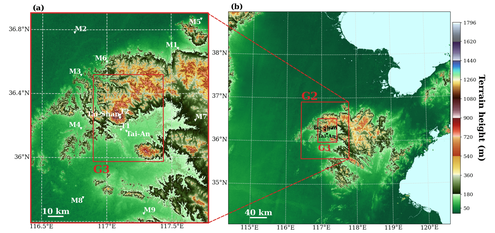

Figure 2: Domains, Surface $\Delta z \approx 30$ m, G3 $\Delta x = 500$ m

Table 1: model setup

Radiation	Chen & Cotton updated every 10 min
terrain smoothing	Reflected Envelope
Turbulent	Mellor-Yamada 2.5 level
Surface submodel	LEAF3 with 7 soil levels
Initialization	The laterally outermost 5 points nudging to ERA5 with 1350-s damping

Methods

- The transformation of terrain-following σ_z coordinate
- The downward extrapolation with roughness sublayer (RSL) effects[1]

$$\frac{\kappa(z-z_d)}{T_*}\frac{\partial T}{\partial z} = \Phi_H \approx \phi_H\left(\frac{z-z_d}{L}\right)\cdot\hat{\phi}_H\left(\frac{z-z_d}{z_*}\right) \quad (2)$$

- The conditions of *a priori* selected valley-wind days[2] using ERA5 and the observed short-wave radiation are given by

$$\left|\frac{\Delta Z_g}{\Delta x}\right| \,\&\, \left|\frac{\Delta Z_g}{\Delta y}\right| \leqslant 4\times 10^{-5} \quad (3a)$$

$$\mathrm{IDI}(j) = \sum_{i=1}^{1440}\frac{DR_{skc}(i\Delta t, j) - DR_{obs}(i\Delta t, j)}{DR_{skc}(i\Delta t, j)} \leqslant 0.35 \quad (3b)$$

$\Rightarrow$ The valley-wind days are 11, 12, 14, 15, 20, 24, 27 and 30 June in 2018 (8 out of 47 days of simulation).

- The **flow reversal occurrences** operationally defined as the component of horizontal wind along terrain aspect sign change at 10 m AGL.
- The numerical implementation of short-wave radiation considering **shading by surrounding terrain**

Model Performance

Table 2: Statistical performance metrics averaged over 13 sites

	MB	ME	FB	NMSE
10-m Wind Direction	-3.24 °	44.88 °	-	0.16
10-m Wind Speed	0.16 m s^{-1}	1.34 m s^{-1}	0.05	0.39
2-m Temperature	-0.44 ℃	1.83 ℃	-0.02	0.01

	MG	R^2	FAC_2	DACC (11.25°)	DACC (22.5°)	DACC (45°)
10-m Wind Direction	-	-	-	0.20	0.38	0.65
10-m Wind Speed	1.07	0.18	0.72	-	-	-
2-m Temperature	1.00	0.71	1.00	-	-	-

Note: MB: the mean bias; ME: the mean error; FB: the fractional bias; NMSE: the normalized mean square error; MG: the geometric mean bias; R^2: the coefficient of determination; FAC_2: the fraction of predictions within a factor of 2 of observations; DACC(45°): the directional accuracy with the threshold of 45°.

Results: Topographic Shading

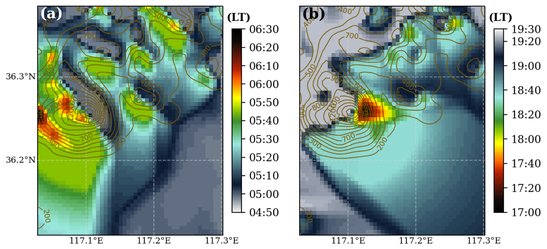

Figure 3: Local (a) sunrise and (b) sunset on 12 June

Results: Flow Reversal

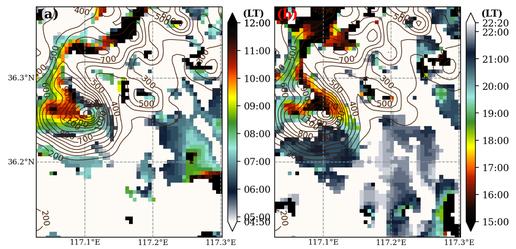

Figure 4: The timing of flow reversal during (a) the morning transition and (b) the evening transition

Self-shadowing for different aspects otherwise following the front formation mechanism

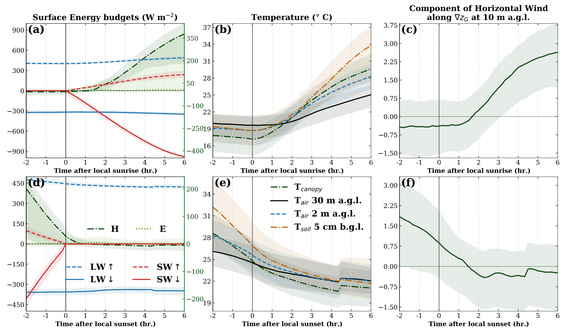

Figure 5: The evolution of land-atmosphere energy-transfer dynamics aligned by the local (a-c) sunrise or (d-f) sunset

Conclusions

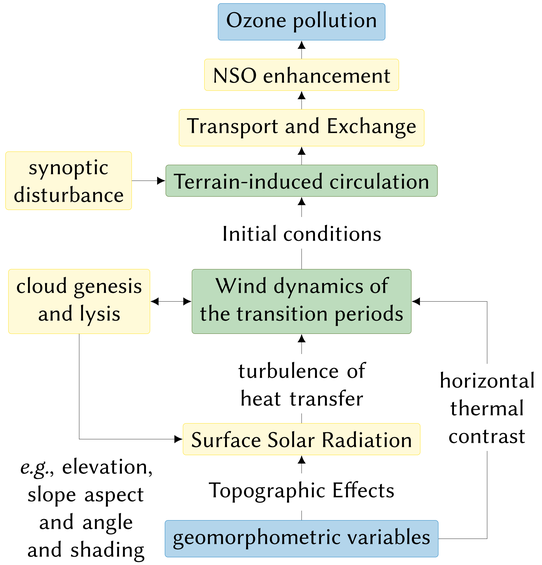

Future Work:

- optimise the horizon algorithm
- further analyse the ozone transport processes with CMAQ
- investigate the effect of subgrid geomorphometric variables on thermally-driven flows

References

[1] K. D. Ridder, "Bulk transfer relations for the roughness sublayer," *Boundary-Layer Meteorology*, vol. 134, pp. 257–267, dec 2009.

[2] M. Lehner, M. W. Rotach, and F. Obleitner, "A method to identify synoptically undisturbed, clear-sky conditions for valley-wind analysis," *Boundary-Layer Meteorology*, vol. 173, pp. 435–450, aug 2019.